ARTICLE INFO
Article ID: 03-16-06-0040

doi:10.4271/03-16-06-0040

Control-Oriented Data-Driven and Physics-Based Modeling of Maximum Pressure Rise Rate in Reactivity Controlled Compression Ignition Engines

Behrouz Khoshbakht Irdmousa,[1] L. N. Aditya Basina,[2] Je!rey Naber,[2] Javad Mohammadpour Velni,[3] Hoseinali Borhan,[4] and Mahdi Shahbakhti[5] AQ01

[1]United States
[2]Michigan Technological University, Mechanical Engineering-Engineering Mechanics Department, USA
[3]University of Georgia, School of Electrical and Computer Engineering, USA
[4]Cummins Inc, USA
[5]University of Alberta, Department of Mechanical Engineering, USA

Abstract

Reactivity controlled compression ignition (RCCI) is a viable low-temperature combustion (LTC) regime that can provide high indicated thermal e"ciency and very low nitrogen oxides (NOx) and particulate matter (PM) emissions compared to the traditional diesel compression ignition (CI) mode [1]. The burn duration in RCCI engines is generally shorter compared to the burn duration for CI and spark-ignition (SI) combustion modes [2, 3]. This leads to a high pressure rise rate (PRR) and limits their operational range. It is important to predict the maximum pressure rise rate (MPRR) in RCCI engines and avoid excessive MPRRs to enable safe RCCI operation over a wide range of engine conditions. In this article, two control-oriented models are presented to predict the MPRR in an RCCI engine. The first approach includes a combined physical and empirical model that uses the first principle of thermodynamics to estimate the PRR inside the cylinder, and the second approach estimates MPRR through a machine learning method based on kernelized canonical correlation analysis (KCCA) and linear parameter-varying (LPV) methods. The KCCA-LPV approach proved to have higher prediction accuracy compared to physics-based modeling while requiring less amount of calibration. The KCCA-LPV approach could estimate MPRR with an average error of 47 kPa/CAD while the physics-based approach's average estimation error was 87 kPa/CAD.

History

Received: 05 May 2022
Revised: 07 Oct 2022
Accepted: 21 Nov 2022

Keywords

RCCI engine, Maximum pressure rise rate, Control-oriented model, Data-driven modeling, Physics-based modeling

Citation

Khoshbakht Irdmousa, B., Basina, L., Naber, J., Mohammadpour Velni, J. et al., "Control-Oriented Data-Driven and Physics-Based Modeling of Maximum Pressure Rise Rate in Reactivity Controlled Compression Ignition Engines," *SAE Int. J. Engines* 16(6):2023, doi:10.4271/03-16-06-0040.

ISSN: 1946-3936
e-ISSN: 1946-3944

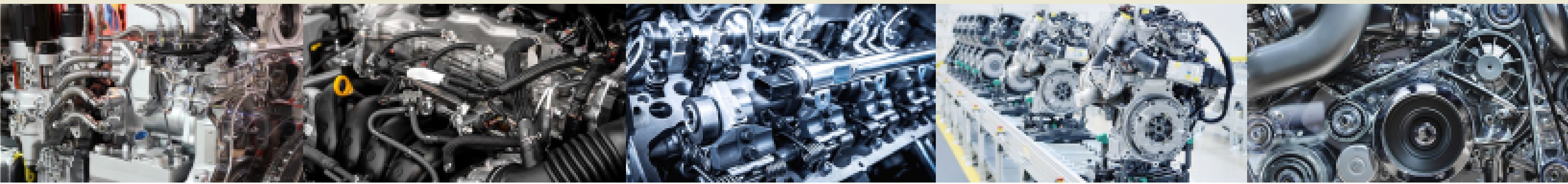

Introduction

AQ02

RCCI combustion is a form of LTC regime, which is designed to operate with a mixture of two fuels with di!erent reactivities. "ese fuels are injected by two sets of injectors to adjust reactivity levels and control the combustion process inside the combustion chamber. Port fuel injectors (PFI) are used to deliver a low reactivity fuel to the intake air#ow while a high reactivity fuel is directly injected inside the combustion chamber. Combustion in RCCI engines initiates at high reactivity fuel–air mixture pockets inside the combustion chamber and then advances to burn the low reactive regions [4]. Since high reactivity pocket formation depends on fuel concentration and local temperature and in-cylinder pressure, it is challenging to control combustion in RCCI engines to achieve low emission and high thermal e$ciency bene%ts. Inadequately controlled RCCI engines may generate high carbon monoxide (CO) and unburned hydrocarbon (UHC) emissions and run with high cyclic variability (COV_{IMEP}) [5]. Control of combustion in RCCI and other LTC regimes have been an active area of research in the past two decades [6, 7, 8, 9, 10, 11]. Moreover, running RCCI engines at high loads poses another challenge regarding high maximum pressure rise rate (MPRR) values. High MPRR occurs at high loads due to fuel mixture homogeneity, which causes the formation of simultaneous autoignitions in regions inside the combustion chamber [12]. "is issue generates high heat release rates and results in high MPRR values, which creates high combustion noise and high ringing intensity (RI) [5].

Several studies have been conducted to model MPRR in internal combustion (IC) engines. Representation of sample of these methods are presented in Figure 1. "ese studies can be categorized into physics-based modelings and data-driven modelings. Physics-based models describe IC engines' cycle through the %rst law of thermodynamics and use calibrated physical models to represent heat transfer, fuel injection, and the combustion process. In contrast, data-driven models use machine learning algorithms to model the relation between measurable IC engine outputs such as load, combustion timing, and controllable engine inputs such as fuel quantity and injection timings [13, 14]. Physics-based modeling studies can be subcategorized into multizone models, computational #uid dynamic (CFD) models, and correlation-based models. Sjöberg et al. [15] developed a multizone model of an HCCI engine and studied the e!ects of thermal strati%cation and combustion retardation on MPRR. "ey found that the high-load operating limit of HCCI engines can be extended by adjusting the thermal stratification. Other researchers including Ozaki et al. [16], Shirota et al. [17], and Jung et al. [18] also estimated MPRR for HCCI engines through a multizone model and studied the e!ects of thermal and mixing strati%cation. "ey con%rmed the positive e!ect of thermal strati%cation on reducing MPRR and expanding the operational range of HCCI engines. Shigetoyo et al. [19] studied MPRR in HCCI engines through developing a multizone model. "ey found that retarding combustion can reduce

FIGURE 1 Sample of previous studies in maximum pressure rise rate modeling and characterization and contributions of this study highlighted in red. Data taken from Ref. [15, 16, 17, 19, 20, 21, 22, 23, 24, 25, 26, 27, 28, 29].

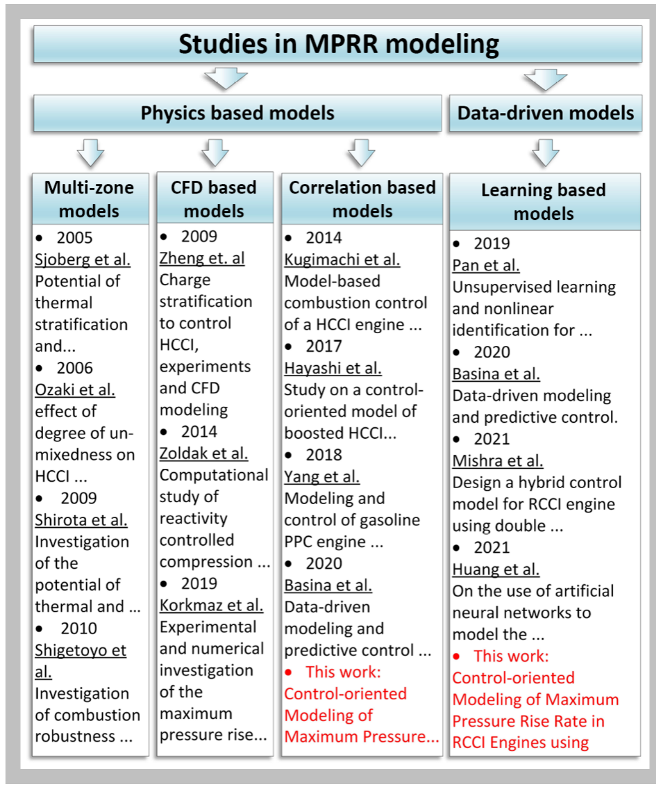

MPRR for HCCI engines, however excessive retardation can reduce combustion robustness.

Other researchers have developed high-fidelity CFD combustion models to study MPRR for IC engines. Zheng et al. [20] used a CFD simulation to model an n-heptane fueled HCCI-like engine and studied the e!ects of charge strati%cation on MPRR. "ey con%rmed the conclusions obtained by multizone modeling and found that increasing the ratio of direct injection to premixed injection creates higher strati%cation and consequently decreases MPRR for HCCI engines. In another CFD study, Zoldak et al. [21] developed a CFD model of an RCCI engine and compared it with conventional diesel operation while considering MPRR as operational constraints for both of them. They found that by satisfying MPRR constrain, RCCI engines can provide 24% decrease in fuel consumption compared to conventional diesel operation when operated at the same rated power, air–fuel ratio (AFR), and exhaust gas recirculation (EGR) rate. Korkmaz et al. [22] also investigated MPRR in RCCI engines using a validated CFD model. "ey studied to reduce MPRR to less than 1 bar/CAD in RCCI engines and expand the operational range by implementing optimum injection strategy.

Multizone and CFD model-based MPRR models are computationally expensive and cannot be used for high-speed applications such as feedback controller design. "erefore, researchers have developed another class of MPRR models, which is the correlation-based model. Kugimachi et&al. [23] represented MPRR for an HCCI engine as a correlation based upon charge composition, temperature, and volume at the end of combustion. "ey also developed a discrete control-oriented model that used a linear quadratic regulator (LQR) strategy to build a combustion controller. Hikita et&al. [24] also built a control-oriented model for the HCCI engine and developed a correlation for MPRR based on the thermodynamic properties of charge at the end of combustion. " ey used this model to build a feedforward load controller for the HCCI engine. Yang et&al. [25] developed a control-oriented model for a gasoline-fueled partially premixed combustion (PPC) engine and used it to structure a PI and an MPC controller to control load and combustion phasing while considering MPRR and emission constraints. " ey presented a correlation for MPRR based on the %rst law of thermodynamics and used a double Wiebe function to characterize heat release. A similar approach for representing MPRR is used by Basina et&al. [26] while developing an LPV-MPC controller for load and combustion phasing in an RCCI engine. "eir controller was able to track CA50 and IMEP without violating allowable MPRR values of 5.8 bar/CAD.

" e physics-based MPRR models require characterization and calibration of a model to represent thermodynamic process inside the combustion chamber, which can be&time-consuming. Researchers recently employed a new data-driven approach to model MPRR, which will either reduce modeling time or increase model accuracy. Pan et&al. [27] developed one of the %rst data-driven MPRR models and used an unsupervised learning process to estimate pressure trace of a diesel engine during the combustion rate shaping (CRS) process. In another work, Basina et&al. [26] developed a data-driven MPRR model using data obtained from an RCCI engine model. "ey built their model using linear parameter-varying (LPV) approach and could estimate transient MPRR with 60&kPa/CAD accuracy. Shin et&al. [30] used a deep learning approach to train and estimate maximum cylinder pressure, the crank angle at maximum cylinder pressure, and MPRR for a gasoline engine. " eir model consisted of seven hidden layers and could estimate MPRR with 2 kPa/CAD as the estimation error. Liu et&al. [31] used a backpropagation arti%cial neural network model to estimate maximum in-cylinder pressure and pressure rise rate (PRR) for an optical gasoline engine. "eir goal was to avoid testing conditions with unsafe maximum pressure and MPRR values for an optical engine. "ey found that a well-trained arti%cial neural network model can provide fast and consistent results, making it an easy-to-use tool for designing future experimental testings for the optical engine. Huang et&al. [28] used arti%cial neural networks to model peak cylinder pressure and its location, MPRR, and indicated mean e!ective pressure for a heavy-duty natural gas spark-ignition engine. Mishra et&al. used random forest machine learning (RFML) approach along a parametrized double Wiebe function to predict MPRR in an RCCI engine. " eir model could estimate MPRR with 1.8 kPa/CAD as the mean estimation error [29]. " ese developed MPRR models can estimate MPRR very accurately, however, they are computationally expensive. Moreover, these models are trained based on steady-state data and plant dynamics was not considered in their modeling approach. Consequently, they are not appropriate for fast control applications due to their high computational load and lack of plant dynamic at identi%cation [28, 30, 31]. Recent works by Maldonado et&al. on real-time implementation of spiking neural networks for SI engine control show promising results. "is approach is a good candidate for real-time MPRR control of RCCI engines due to its low computational load [32, 33, 34].

Extension of high load operation in RCCI engines requires an active MPRR control strategy based on a fast control-oriented MPRR model. "is article proposes two new control-oriented MPRR models in RCCI engines that are trained with a wide range of experimental transient data. " ese models can be&used to control MPRR and extend the high load operation of RCCI engines.

" is article is organized as follows. " e experimental RCCI engine setup is described in Section II. " en, the %rst control-oriented MPRR model using Wiebe-based modeling is described in Section III. Subsequently, the algorithm to develop a data-driven KCCA-LPV model for MPRR estimation is given in Section IV. Finally, a summary of results and comparison between the two MPRR models is provided.

Experimental!Setup

" is research utilized a 2.0L GM Ecotec engine in the Energy Mechatronics Laboratory (EML) at the Michigan Tech's Advanced Propulsion Systems (APS) Research Center. " e experimental setup layout and view are presented in Figure 2. " e speci%cations of the engine are given in Table 1. " e engine is equipped with PFI and DI injectors to enable RCCI operation. " e PFI fuel system is used to deliver iso-octane as the low reactivity fuel while the DI fuel system is used to deliver n-heptane as the high reactivity fuel. "e ratio between low reactive fuel and high reactivity fuel is characterized by the premixed ratio (PR). It is de%ned based on chemical energy from the low reactive fuel divided by the total chemical energy delivered by both fuels and calculated according to Equation 1.

$$PR = \frac{m_{isooctane} LHV_{isooctane}}{m_{isooctane} LHV_{isooctane} + m_{nheptane} LHV_{nheptane}}. \quad \text{Eq. (1)}$$

where LHV represents lower heating value of fuels and m represents injected fuel mass per cylinder.

" e engine is connected to a 460 hp AC dynamometer. A dSPACE MicroAutoBox unit is used as an engine control unit while a dSPACE RapidPRo unit provides power and control signals to actuators. Due to the sensitivity of RCCI operation to intake air temperature, a controllable air heater is included to warm the intake air#ow to desired temperatures. " e pressure trace from the engine is collected by a combustion analysis system (CAS) at 0.1 CAD resolution and then provided to a Xilinx programmed Spartan-6 %eld FPGA unit to compute real-time MPRR. "e experimental pressure traces

FIGURE 2 RCCI engine experimental setup: (a) layout, (b) real setup overview.

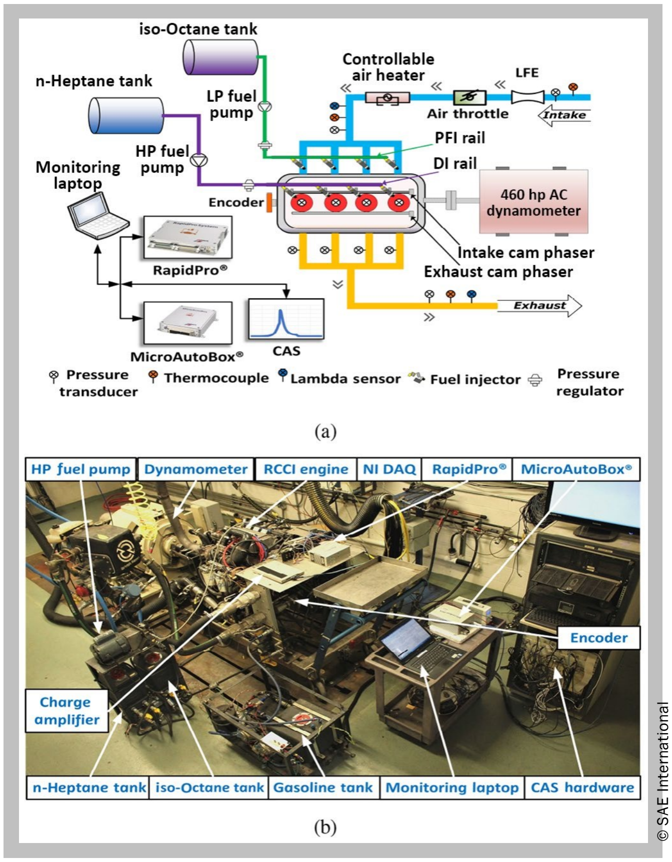

from this engine are used to obtain MPRR based on PRRs at 0.1 crank angle intervals. " e computed MPRRs are later utilized for MPRR model development and validation. Figure 3 presents a sample of experimental data set obtained by operating the RCCI engine with a series of input fuel quantity (FQ), the start of injection (SOI), and PR. Iso-octane and n-heptane were injected based on corresponding FQ, PR, and SOI values for each cycle, and pressure trace and encoder output were recorded and used to compute MPRR for the cycle.

Empirical Wiebe-Based MPRR Model

Empirical Wiebe-driven MPRR modeling is a physics-based method used to develop a control-oriented MPRR correlation [25]. " is article develops the %rst MPRR model in RCCI engines using transient experimental data, which can be used to estimate MPRR in RCCI engines based on the control actions. "is model requires the development of an in-cylinder PRR model. Pressure rise rate can be computed using the %rst law of thermodynamics as presented in Equation 2 [35]

$$\frac{dP}{d\theta}=\frac{\gamma-1}{V}\left(\frac{dQ}{d\theta}-\frac{dQ_w}{d\theta}\right)-\frac{\gamma P}{V}\cdot\frac{dV}{d\theta} \qquad \text{Eq. (2)}$$

TABLE 1 Engine specifications.

Make	General Motors
Model	Ecotec 2.0 L Turbocharged
Engine type	4 stroke, 4 cylinders
Fuel system	Direct and port fuel injection
Displaced volume	1998 [cc]
Bore	86 [mm]
Stroke	86 [mm]
Compression ratio	9.2:1
Max. engine power	164 at 5300 [kW at rpm]
Max. engine torque	353 at 2400 [Nm at rpm]
Firing order	1-3-4-2
IVO	25.5/−24.5 [°CAD bTDC]
IVC	2/−48 [°CAD bBDC]
EVO	36/−14 [°CAD bBDC]
EVC	22/−28 [°CAD bTDC]
Valve lift	10.3 [mm]

where $\frac{dQ}{d\theta}$ represents the rate of heat release, γ is the ratio of speci%c heats, P is the instantaneous pressure, V is the instantaneous volume, and $\frac{dQ_w}{d\theta}$ is the heat transfer to the wall computed through the Woschni heat transfer model [36].

Heat release from the fuel is linearly correlated with mass fraction burn (MFB) of the fuel. MFB can be modeled using a single-term or a double-term Wiebe function presented at Equations 3 and 4, respectively [35]

$$X_b(\theta)=1-\exp\left[-\left(\frac{\theta-\theta_{soc}}{\alpha\,\Delta\theta}\right)^m\right]. \qquad \text{Eq. (3)}$$

FIGURE 3 Experimental data from RCCI engine at T_{in} = 333 K, N = 1200 RPM, P_{in} = 96.5 kPa.

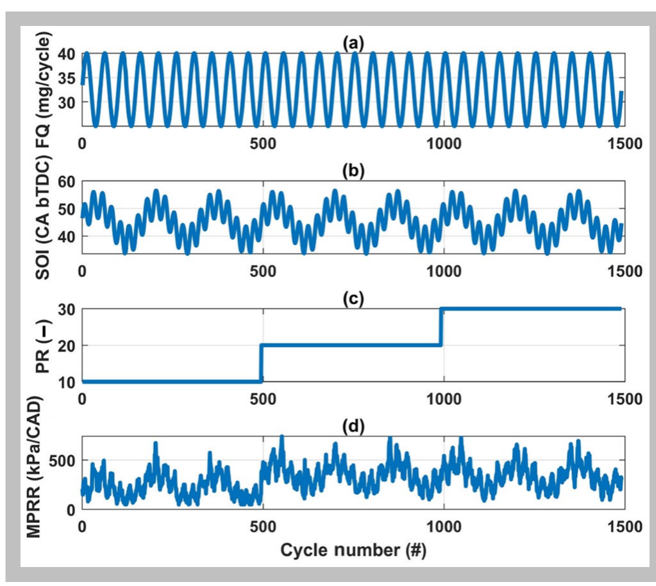

$$X_b(\theta) = \lambda\left[1 - \exp\left[-\left(\frac{\theta - \theta_{soc}}{\alpha_1 \Delta\theta}\right)^{m_1}\right]\right] + (1-\lambda)\left[1 - \exp\left[-\left(\frac{\theta - \theta_{soc}}{\alpha_2 \Delta\theta}\right)^{m_2}\right]\right]. \quad \text{Eq. (4)}$$

where X_b is the mass fraction burned, θ is the instantaneous angle, θ_{soc} is the crank angle at the start of combustion, "θ is the combustion duration, λ is the fraction of the mixture that burns in the fast combustion stage, and α, m, m_1, m_2 are calibration parameters.

Figure 4 presents PRR values throughout cycle for the transient experimental data presented in Figure 3. Mass fraction burnt data for the same transient data is also presented in Figure 5. It can be&observed that MPRR happens less than 15 CAD a’er the start of combustion (SOC). Based on the comparison between the MFB estimation of a single-term and a double-term Wiebe function, which is presented in Figure 6, the double-term Wiebe function estimates experimental MFB accurately for the entire combustion process. However, the single-term Wiebe function’s accuracy is limited to angles close to the SOC.

Since MPRR happens close to SOC, either a single-term or a double-term Wiebe function can be&used to represent experimental MFB. " e single-term Wiebe function as given in Equation 3 is preferred in this work due to the simplicity of its calibration compared to a double-term Wiebe function.

" e Wiebe function combined with the LHV of the fuels is used to present the fuel heat release rate form as

$$\frac{dQ}{d\theta} = LHV_{eff}\,\frac{m}{\alpha\,\Delta\theta}\left(\frac{\theta - \theta_{soc}}{\Delta\theta}\right)^{(m-1)} \exp\left[-\left(\frac{\theta - \theta_{soc}}{\alpha\,\Delta\theta}\right)^{m}\right] \quad \text{Eq. (5)}$$

" e lower heating value of fuels is denoted by $LHV_{e\%}$ and is calculated by

$$LHV_{eff} = (1 - PR) \times LHV_{DI} + PR \times LHV_{PFI}, \quad \text{Eq. (6)}$$

FIGURE 4 Experimental pressure rise rate for transient cycles, *N* = 1000 RPM, T_{in} = 333!K.

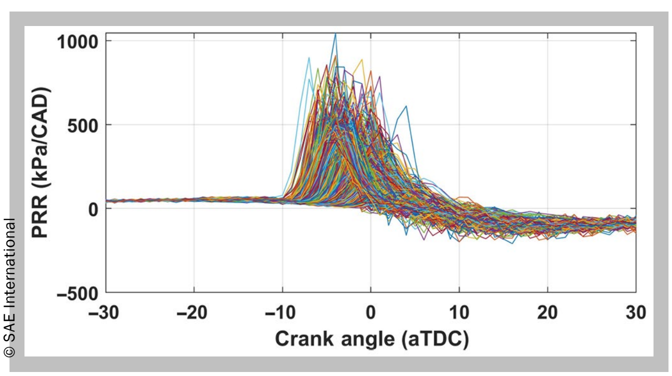

FIGURE 5 Experimental mass burnt fraction for transient cycles, *N* = 1000 RPM, T_{in} = 333!K.

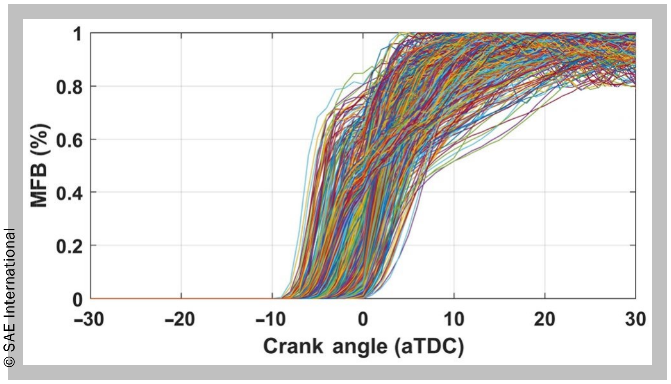

where LHV_{DI} represents the lower heating value of the DI’s injected fuel, in this case, n-heptane, and LHV_{PFI} is the LHV of the PFI injected fuel, in this case, iso-octane.

Accurate MPRR estimation requires calibration of Equation 3 as the Wiebe function used for MFB estimation. Calibration parameters are m as the shape factor and "θ as the burn duration, which are described by the following equations [26]

$$m = C_1' + C_2' \times (1+K) \times SOI + C_3' \times K \quad \text{Eq. (7)}$$

$$\Delta\theta = C_1 + K\left(C_2 \times \phi_{di} + C_3 \times \phi_{pfi} + C_4 \times SOI + C_5\right) + C_4 \times SOI \quad \text{Eq. (8)}$$

in which K is as follows:

$$K = \exp\left[-(SOI - C_6)^{C_7}\right]. \quad \text{Eq. (9)}$$

Equations 7 to 9 are parameterized using transient experimental data collected from the RCCI engine with 1500 consecutive cycles; 65% of these points, i.e., 975 data points were used to parametrize the Wiebe function while the rest, i.e., 525 data points, were used to test the calibrated Wiebe function.

FIGURE 6 Experimental mass fraction burn estimation, FQ = 17 mg/cycle, SOI = 40 CAD bTDC, *N* = 1000 RPM, T_{in} = 333!K.

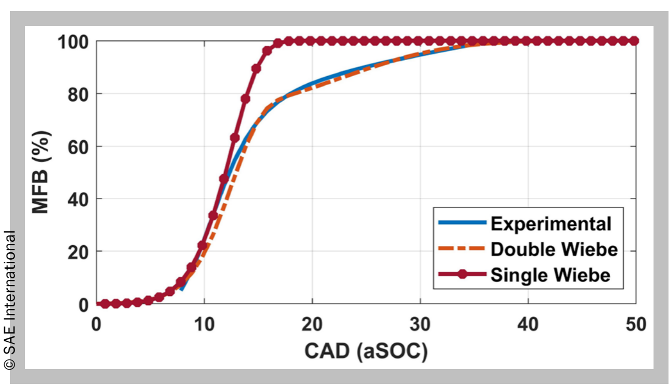

FIGURE 7 Time histories of FQ and SOI for the test data at N = 1000 RPM, T_{in} = 333 K.

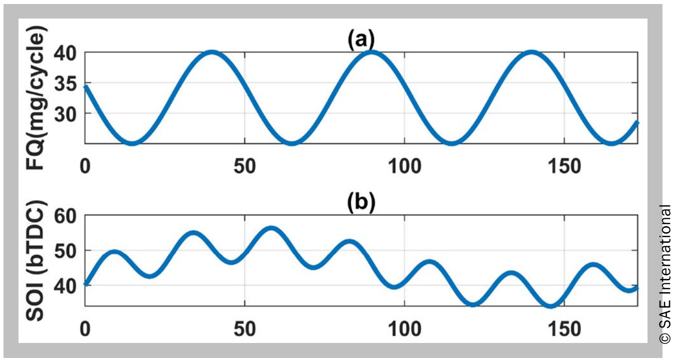

FIGURE 9 Effect of unknown states number on KCCA-driven MPRR model prediction accuracy.

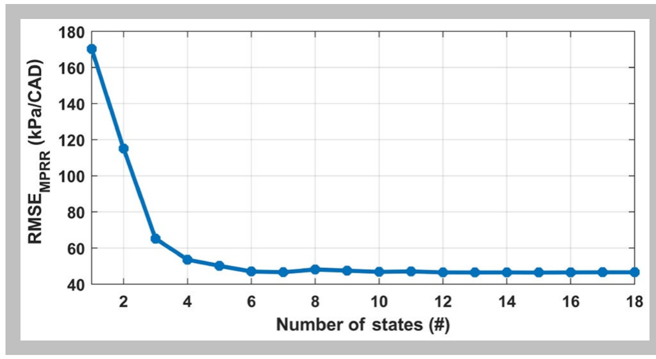

Calibrated MPRR model was then used to estimate MPRR for the test dataset. Figure 7 presents time history of FQ and SOI at test data set. Experimental test dataset and modeled MPRR for three experimental datasets are presented in Figure 8. It can be observed that the MPRR model was able to predict experimental MPRRs with the root mean squared error (RMSE) of 87 kPa/CAD. The Wiebe-based MPRR model could only estimate the general trend of test data. This is due to the static structure of this model, which does not consider the effect of engine inputs at previous cycles on the current cycle MPRR value. This problem will be addressed in the next section by implementing a dynamic state-space KCCA-LPV structure.

FIGURE 8 Performance of the Wiebe-based approach to model MPRR for the test data at N = 1000 RPM, T_{in} = 333 K, (a) PR = 12, (b) PR = 18, (c) PR = 24.

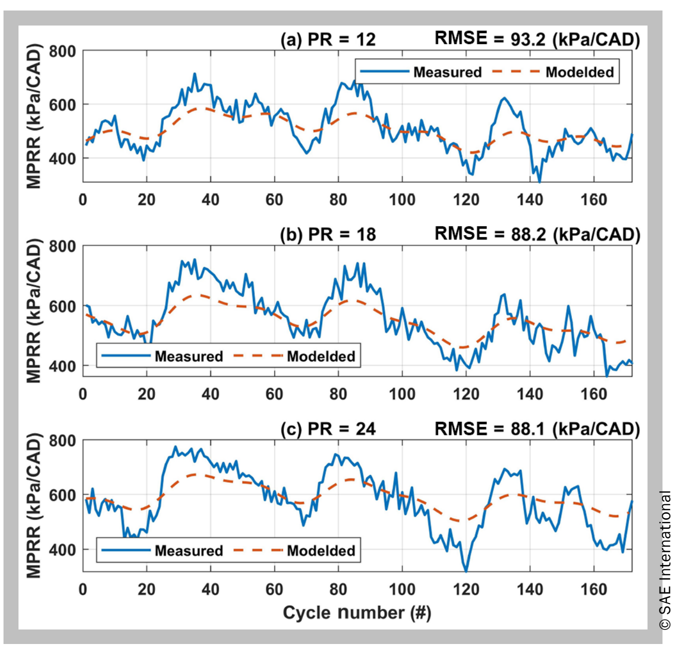

KCCA-Driven MPRR Model

This section presents the second approach to model MPRR in RCCI engines using a data-driven approach. Data-driven modeling approaches can provide a reasonably accurate estimation without prior knowledge. This provides significant modeling flexibility and significantly accelerates the modeling process for an unknown phenomenon compared to physics-based models, which require accurate physical understanding and modeling. Therefore, a data-driven approach based on kernelized canonical correlation analysis (KCCA) is employed in this section to obtain data-driven modeling benefits. Moreover, the KCCA method enables plant states to be independent of the plant outputs, which allows states' numbers to be adjusted to reach the highest accuracy of the data-driven model. This study adopts the state estimation approach developed by Rizvi et al. [37] and generates KCCA combustion model based on implemented engine inputs and measured engine outputs. A state-space dynamic model for a LPV system can be presented as

$$X_{k+1} = A(p_k)X_k + B(p_k)U_k + K(p_k)E_k, \quad \text{Eq. (10a)}$$

$$Y_k = C(p_k)X_k + E_k, \quad \text{Eq. (10b)}$$

where U_k and Y_k denotes the inputs and outputs, respectively, and X_k represents unknown states vector at moment k. Matrices $A(p_k)$, $B(p_k)$, $K(p_k)$, and $C(p_k)$ represent LPV state-space matrices that are generally dependent on scheduling variables p_k; E_k denotes additive Gaussian white noise. Equation 10 can be rewritten as $E_k = Y_k - C(p_k)X_k$ to form the state-space model as follows

$$X_{k+1} = \tilde{A}(p_k)X_k + \tilde{B}(p_k)U_k + K(p_k)E_k, \quad \text{Eq. (11a)}$$

$$Y_k = C(p_k)X_k + E_k, \quad \text{Eq. (11b)}$$

where $\tilde{A}(p_k) = B(p_k) - K(p_k)D(p_k)$ and $\tilde{B}(p_k) = A(p_k) - K(p_k)C(p_k)$. Identification of $\tilde{A}(p_k)$, $\tilde{B}(p_k)$, $K(p_k)$, and

$C(p_k)$ requires estimation of states (X_k) associated with measured data, i.e., U_k, Y_k. State-space LPV (LPV-SS) formulation of Equation 11 can be used to obtain future outputs as

$$\begin{bmatrix} Y_k \\ Y_{k+1} \\ \vdots \\ Y_{k+d+1} \end{bmatrix} = \left(\mathcal{O}_f^d \diamond p\right)_k X_k + \left(\mathcal{H}_f^d \diamond p\right)_k \begin{bmatrix} U_k \\ U_{k+1} \\ \vdots \\ U_{k+d+1} \end{bmatrix} + \left(\mathcal{L}_f^d \diamond p\right)_k \begin{bmatrix} Y_k \\ Y_{k+1} \\ \vdots \\ Y_{k+d+1} \end{bmatrix} + \begin{bmatrix} e_k \\ e_{k+1} \\ \vdots \\ e_{k+d+1} \end{bmatrix}, \quad \text{Eq. (12)}$$

in which $\left(\mathcal{O}_f^d \diamond p\right)_k$ is the observability matrix at time instant k along with the scheduling trajectory p, $\left(\mathcal{H}_f^d \diamond p\right)_k$ is a forward Toeplitz matrix, and $\left(\left(\mathcal{L}_f^d \diamond p\right)_k\right.$ is a lower triangle matrix. Future measured outputs, inputs, noise, and scheduling parameter vectors for time instant k are collected to form the following matrices

$$\bar{Y}_{k+d}^d := \left[Y_k^\top \ldots Y_{k+d-1}^\top\right]^\top, \quad \text{Eq. (13a)}$$

$$\bar{U}_{k+d}^d := \left[U_k^\top \ldots U_{k+d-1}^\top\right]^\top, \quad \text{Eq. (13b)}$$

$$\bar{E}_{k+d}^d := \left[e_k^\top \ldots e_{k+d-1}^\top\right]^\top, \quad \text{Eq. (13c)}$$

$$\bar{P}_{k+d}^d := \left[p_k^\top \ldots p_{k+d-1}^\top\right]^\top, \quad \text{Eq. (13d)}$$

where d denotes the future data window size. Equation 12 can be rewritten using Equation 13 as

$$\bar{Y}_{k+d}^d = \left(\mathcal{O}_f^d \diamond p\right)_k X_k + \left(\mathcal{H}_f^d \diamond p\right)_k \bar{U}_{k+d}^d + \left(\mathcal{L}_f^d \diamond p\right)_k \bar{Y}_{k+d}^d + \bar{E}_{k+d}^d. \quad \text{Eq. (14)}$$

Unknown states at time step k based on future inputs and outputs are computed from Equation 14 and given as

$$X_k = \left(\mathcal{O}_f^d \diamond p\right)_k^\dagger \left(\left(I - \left(\mathcal{L}_f^d \diamond p\right)_k\right)\bar{Y}_{k+d}^d - \left(\mathcal{H}_f^d \diamond p\right)_k \bar{U}_{k+d}^d\right) - \left(\mathcal{O}_f^d \diamond p\right)^\dagger \bar{E}_{k+d}^d. \quad \text{Eq. (15)}$$

Since E is an independent zero-mean process noise, which is identically distributed for our experimental data, $\left(\mathcal{O}_f^d \diamond p\right)^\dagger \bar{E}_{k+d}^d$ is expected to be zero and can be eliminated. State estimation represented by Equation 15 is simplified to Equation 16 by defining $Z_{k+d}^d = \begin{bmatrix} \bar{U}_{k+d}^d \\ \bar{Y}_{k+d}^d \end{bmatrix}$ as the collection of future inputs and outputs:

$$X_k = \left(\mathcal{O}_f \diamond p\right)_k^\dagger \left[-\left(\mathcal{H}^d \diamond p\right)_k \quad I - \left(\mathcal{L}_f^d \diamond p\right)_k\right] \bar{Z}_{k+d}^d. \quad \text{Eq. (16)}$$

Future mapping matrix can be defined as

$$\varphi_f\left(\bar{p}_{k+d}^d\right) = \left(\mathcal{O}_f \diamond p\right)_k^\dagger \left[-\left(\mathcal{H}^d \diamond p\right)_k \quad I - \left(\mathcal{L}_f^d \diamond p\right)_k\right], \quad \text{Eq. (17)}$$

and state estimation at time step k can be simply expressed as

$$X_k = \varphi_f\left(\bar{p}_{k+d}^d\right)\bar{Z}_{k+d}^d. \quad \text{Eq. (18)}$$

This approach is also applicable to past measurements to estimate unknown states at time step k based on step-wise output calculation from past d step measurements as

$$X_k = \left(\mathcal{X}_p^d \diamond p\right)_k X_{k-d} + \left(\mathcal{R}_p^d \diamond p\right)_k \begin{bmatrix} U_{k-d} \\ U_{k-d+1} \\ \vdots \\ U_{k-1} \end{bmatrix} + \left(\mathcal{V}_p^d \diamond p\right)_k \begin{bmatrix} Y_{k-d} \\ Y_{k-d+1} \\ \vdots \\ Y_{k-1} \end{bmatrix}. \quad \text{Eq. (19)}$$

Past measured outputs, inputs, noise, and scheduling parameter vectors for time instant k are denoted by $\bar{Y}_k^d$, $\bar{U}_k^d$, $\bar{E}_k^d$, and $\bar{P}_k^d$ and can be computed similar to future data defined at Equation 13. These definitions can be used to rewrite state estimation as

$$X_k = \left(\mathcal{X}_p^d \diamond p\right)_k X_{k-d} + \left(\mathcal{R}_p^d \diamond p\right)_k \bar{U}_k^d + \left(\mathcal{V}_p^d \diamond p\right)_k \bar{Y}_k^d. \quad \text{Eq. (20)}$$

Choosing d such that $\left(\chi_p^d \diamond p\right)_k \approx 0$ and defining $Z_k^d = \begin{bmatrix} \bar{U}_k^d \\ \bar{Y}_k^d \end{bmatrix}$, state estimation in Equation 20 is expressed as

$$X_k = \left[\left(\mathcal{R}_f^d \diamond p\right)_k \quad \left(\mathcal{V}_f^d \diamond p\right)_k\right] \bar{Z}_k^d. \quad \text{Eq. (21)}$$

State estimation at time step k based on the past data is simplified to the following by defining $\varphi_p\left(\bar{P}_k^d\right)$ as the past mapping matrix

$$\varphi_p\left(\bar{P}_k^d\right) = \left[\left(\mathcal{R}_f^d \diamond p\right)_k \quad \left(\mathcal{V}_f^d \diamond p\right)_k\right], \quad \text{Eq. (22)}$$

$$X_k = \varphi_p\left(\bar{P}_k^d\right)\bar{Z}_k^d. \quad \text{Eq. (23)}$$

The past data-based state estimation approach shown in Equation 18 can be employed to obtain a collection of all estimated states at all time steps. This collection is named Φ_p and defined as

$$\Phi_p := \left[\varphi_p\left(\bar{P}_1^d\right)\bar{Z}_1^d \quad \varphi_p\left(\bar{P}_2^d\right)\bar{Z}_2^d \quad \ldots \quad \varphi_p\left(\bar{P}_N^d\right)\bar{Z}_N^d\right]^\top. \quad \text{Eq. (24)}$$

Similarly, Φ_f is defined as the collection of estimated states at all time steps based on the future data estimation method as

$$\Phi_f = [\varphi_p\left(\bar{P}_{1+d}^d\right)Z_{1+d}^d \quad \varphi_p\left(\bar{P}_{2+d}^d\right)Z_{2+d}^d \quad \ldots \quad \varphi_p\left(\bar{P}_{N+d}^d\right)\bar{Z}_{N+d}^d]^\top. \quad \text{Eq. (25)}$$

Past data-based estimated states (Φ) and future data-based estimated states (Φ_f) should ideally be identical. However, due to measurement uncertainties and modeling estimations, they tend to be different. Maximizing correlation between $\#_p$ and $\#_f$ can be&accomplished by canonical correlation analysis (CCA) method. " e CCA problem for $\#_p$ and $\#_f$ can be&formulated as

$$\max_{v_j,w_j} v_j^\top \Phi_f^\top \Phi_p w_j \quad s.t. \quad v_j^\top \Phi_f^\top \Phi_f v_j = w_j^\top \Phi_p^\top \Phi_p w_j = 1 \qquad \text{Eq. (26)}$$

Equation 27 presents the CCA optimization problem in a regularized setting based on an LS-SVM formulation.

$$\max_{v_j,w_j,s,r} J\left(v_j,w_j,s,r\right)=\gamma\sum_{k=1}^{N}\left(s_k r_k - v_f\frac{1}{2}s_k^2 - v_p\frac{1}{2}r_k^2\right)-\frac{1}{2}v_j^\top v_j-\frac{1}{2}w_j^\top w_j$$

$$s.t. \quad s_k = v_j^\top \varphi_f\left(\bar{P}^d_{k+d}\right)\bar{Z}^d_{k+d} \quad r_k = w_j^\top \varphi_p\left(\bar{P}^d_k\right)\bar{Z}^d_k. \qquad \text{Eq. (27)}$$

Solution for the regularized CCA problem can be&obtained by forming Lagrangian as

$$L\left(v_j,w_j,s,r\right) = J\left(v_j,w_j,s,r\right)-\sum_{k=1}^{N}\eta_j^k\left(s_k - v_j^\top \varphi_f\left(\bar{P}^d_{k+d}\right)\bar{Z}^d_{k+d}\right) - \sum_{k=1}^{N}\kappa_j^k\left(s_k - v_j^\top \varphi_f\left(\bar{P}^d_k\right)\bar{Z}^d_k\right), \qquad \text{Eq. (28)}$$

where $\eta_j = \left[\eta_j^1 \ \dots \ \eta_j^N\right]^\top$ and $\kappa_j = \left[\kappa_j^1 \ \dots \ \kappa_j^N\right]^\top$ are Lagrange multipliers. Since the problem is in a convex form, the global minimum is computed where derivatives for Lagrangian function variables are zero. "e problem presented at Equation 26 can be&converted to the following generalized eigenvalue problem

$$K_p p\kappa_j = \lambda_j\left(v_f K_f f + I\right)\eta_j, \qquad \text{Eq. (29a)}$$

$$K_f f\eta_j = \lambda_j\left(v_f K_f f + I\right)\kappa_j, \qquad \text{Eq. (29b)}$$

where $K_{pp} = \Phi_p \Phi_p^\top$ and $K_{ff} = \Phi_f \Phi_f^\top$. Lagrangian multipliers are the solution of the generalized eigenvalue problem below

$$\begin{bmatrix} 0 & K_{pp} \\ K_{ff} & 0 \end{bmatrix}\begin{bmatrix} \eta_j \\ \kappa_j \end{bmatrix} = \lambda \begin{bmatrix} v_{ff}K_{ff}+I & 0 \\ 0 & v_p K_{pp}+I \end{bmatrix}\begin{bmatrix} \eta_j \\ \kappa_j \end{bmatrix}. \qquad \text{Eq. (30)}$$

Finally, the computed Lagrangian multipliers are used to calculate the estimated states as

$$x_k^j = \kappa_j \begin{bmatrix} \left(\bar{Z}^d_1\right)^T \bar{k}\left(\bar{P}^d_1,\bar{P}^d_k\right) \\ \left(\bar{Z}^d_2\right)^T \bar{k}\left(\bar{P}^d_2,\bar{P}^d_k\right) \\ \vdots \\ \left(\bar{Z}^d_N\right)^T \bar{k}\left(\bar{P}^d_N,\bar{P}^d_k\right) \end{bmatrix} = \eta_j \begin{bmatrix} \left(\bar{Z}^d_{1+d}\right)^T \bar{k}\left(\bar{P}^d_{1+d},\bar{P}^d_{k+d}\right) \\ \left(\bar{Z}^d_{2+d}\right)^T \bar{k}\left(\bar{P}^d_{2+d},\bar{P}^d_{k+d}\right) \\ \vdots \\ \left(\bar{Z}^d_{N+d}\right)^T \bar{k}\left(\bar{P}^d_{N+d},\bar{P}^d_{k+d}\right) \end{bmatrix}. \qquad \text{Eq. (31)}$$

" e second step in data-driven MPRR modeling is to use estimated states through the KCCA method along with measured inputs and outputs to obtain a state-space dynamic model of the RCCI engine through a LPV identi%cation. " i s article utilizes least-squared SVM (LS-SVM) to determine matrices $A(p_k)$, $B(p_k)$, $C(p_k)$, and $K(p_k)$ in Equation 11. "ese state-space matrices are de%ned based on support vector weighting matrices and feature maps using the equations presented in Equation 32

$$A(p_k) = W_1\Phi_1(p_k); \quad B(p_k) = W_2\Phi_2(p_k), \qquad \text{Eq. (32a)}$$

$$K(p_k) = W_3\Phi_3(p_k); \quad C(p_k) = W_4\Phi_4(p_k), \qquad \text{Eq. (32b)}$$

where unknown support vector weighting matrices are shown by $W_{1;2;3;4}$ and unknown feature maps are represented by $\#_{1;2;3;4}$. An SVM-based discrete-time state-space model can be&represented by

$$X_{k+1} = W_1\Phi_1(p_k)X_k + W_2\Phi_2(p_k)U_k + W_3\Phi_3(p_k)Y_k, \qquad \text{Eq. (33a)}$$

$$Y_k = W_4\Phi_4(p_k)X_k. \qquad \text{Eq. (33b)}$$

State-space matrices can be&obtained from feature maps and weighting matrices as follows based on the approach presented by Rizivi et&al. [38]

$$A_e(\times) = W_1\Phi_1(\times) = \sum_{k=1}^{N}\alpha_k x_k^T \bar{k}^1(p_k,\times), \qquad \text{Eq. (34a)}$$

$$B_e(\times) = W_2\Phi_2(\times) = \sum_{k=1}^{N}\alpha_k u_k^T \bar{k}^2(p_k,\times), \qquad \text{Eq. (34b)}$$

$$K_e(\times) = W_3\Phi_3(\times) = \sum_{k=1}^{N}\alpha_k y_k^T \bar{k}^3(p_k,\times), \qquad \text{Eq. (34c)}$$

$$C_e(\times) = W_4\Phi_4(\times) = \sum_{k=1}^{N}\beta_k x_k^T \bar{k}^3(p_k,\times), \qquad \text{Eq. (34d)}$$

where α and β are Lagrangian multipliers of the LS-SVM optimization problem, and $\bar{k}^i\left(p_j,p_k\right)$ is Gaussian kernel function de%ned as

$$\bar{k}_i\left(p_j,p_k\right) = \exp\left(-\frac{\left\|p_j - p_k\right\|_2^2}{2\sigma_i^2}\right), \qquad \text{Eq. (35)}$$

where σ_i denotes the standard deviation and $||.||_2$ is the l_2 norm. " e de%ned Gaussian function is used in our LPV modeling approach to perform the so-called kernel trick. Computed matrices $A_e(.)$, $B_e(.)$, $K_e(.)$, and $C_e(.)$ in Equation 34 can be&substituted into Equation 3 to represent the data-driven state-space dynamic model of the plant.

" e described data-driven method was implemented on the experimental data collected from the RCCI engine. " e input PR, FQ, and n-heptane SOI were varied and MPRR was computed from acquired pressure traces data. Figure 3 presents a sample of the experimental data obtained from the RCCI engine. " e collected experimental data were divided into training and test datasets. " e training dataset, which consists of 65% of data, is used to train the KCCA-LPV model and the remaining 35% is reserved as the test data. In this work, the effect of the number of states at the dynamic state-space model on MPRR estimation accuracy is also studied. Figure 9 presents the e!ect of unknown state numbers on estimation accuracy. It can be&observed that by increasing the number of states, estimation error decreases and reaches an almost constant value. In this article, the number of unknown states is selected to be&six where high estimation accuracy can be&achieved while avoiding the high computational cost associated with using higher state numbers. " e state-space dynamic model of the MPRR is structured and presented in Equation 36. Dependency of the identi%ed $\mathring{A}_e$ and B_e matrices on the FQ as the scheduling parameter is shown in Figure 10. Elements of these matrices represent an almost linear trend per FQ variation. " e y also have a relatively large range of variation. " e s e characteristics demonstrates that the identi%ed model is a LPV representation of the MPRR dynamics in the RCCI engine.

$$\begin{bmatrix} X_1 \\ X_2 \\ X_3 \\ X_4 \\ X_5 \\ X_6 \end{bmatrix}_{(k+1)} = \mathring{A}_e(FQ) \begin{bmatrix} X_1 \\ X_2 \\ X_3 \\ X_4 \\ X_5 \\ X_6 \end{bmatrix}_{(k)} + B_e(FQ) \begin{bmatrix} FQ \\ SOI \\ PR \end{bmatrix}_{(k)} \quad \text{Eq. (36a)}$$

$$[MPRR]_{(k+1)} = C(FQ)\,[X_1 X_2 X_3 X_4 X_5 X_6]^T_{(k+1)}, \quad \text{Eq. (36b)}$$

FIGURE 10 Dependency of the elements of the identified *A* and *B* matrices (of the learned LPV model) on the scheduling parameter (FQ).

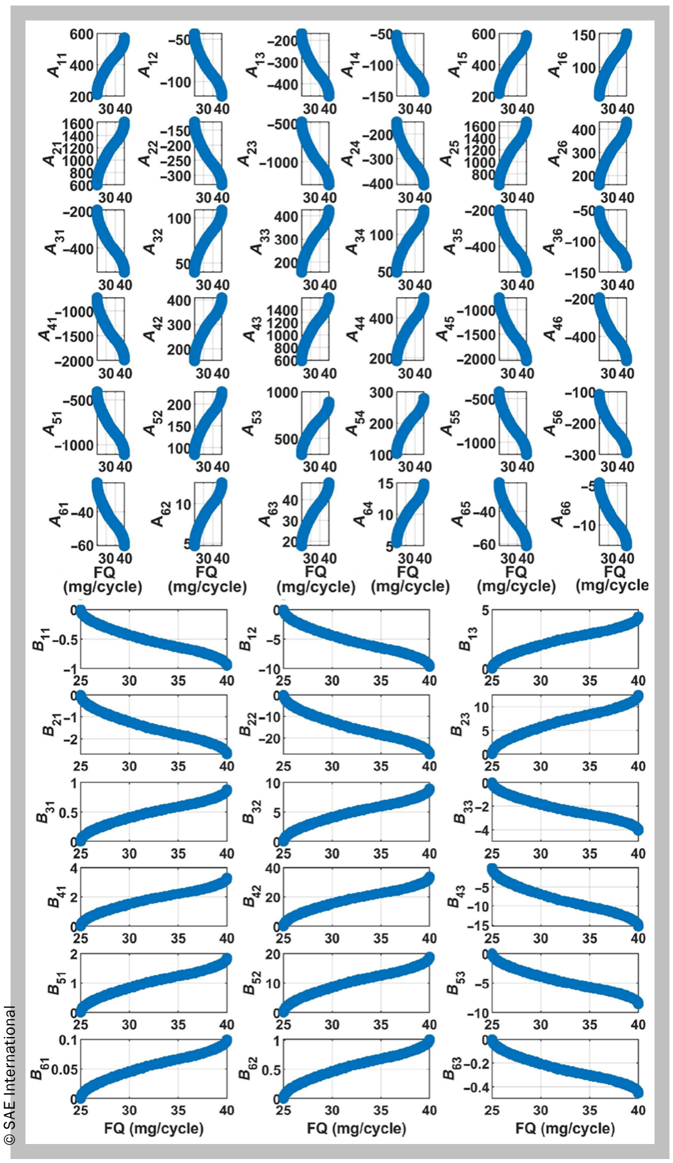

"e developed KCCA-LPV model is then used to estimate the experimental MPRR values. Figure 11 presents estimation results for the learned KCCA model for the test data at three PR values. It demonstrates that the LPV model can estimate the experimental MPRRs with an average estimation error of 45 kPa/CAD. Figure 12 presents the comparison between MPRR estimation of the two models at PR = 14, PR = 20, and PR = 18. "e root mean square error of the Wiebe-based model is 64 kPa/CAD, 67 kPa/CAD, and 87 kPa/CAD for PR = 14, PR = 20, and PR = 28, respectively. On the other hand, the data-driven model could estimate the experimental data at PR = 14, PR = 20, and PR = 28 with an average error of 28 kPa/CAD, 29 kPa/CAD, and 48 kPa/CAD.

It can be&observed that the data-driven method can estimate the measured MPRR values with better accuracy compared to the Wiebe-based method while requiring less development time due to its #exible modeling characteristics.

FIGURE 11 Performance of the KCCA-driven model to estimate MPRR for the test data at T_{in} = 333 K, N = 1200 RPM, P_{in} = 96.5 kPa and (a) PR = 12, (b) PR = 18, (c) PR = 24.

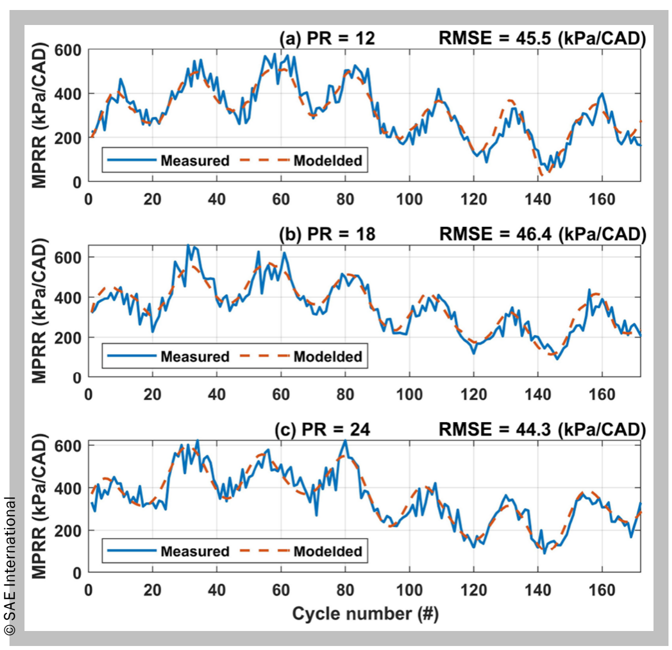

FIGURE 12 Estimation performance of the Wiebe-based and KCCA-driven MPRR models at T_{in} = 333 K, N = 1200 RPM, P_{in} = 96.5 kPa (a) PR = 14, RMSE Wiebe-based = 64 kPa/CAD, RMSE KCCA-Driven = 28 kPa/CAD (b) PR = 20, RMSE Wiebe-based = 67 kPa/CAD, RMSE Data-Driven = 29 kPa/CAD. (c) PR = 28, RMSE Wiebe-based = 88 kPa/CAD, RMSE KCCA-Driven = 48 kPa/CAD.

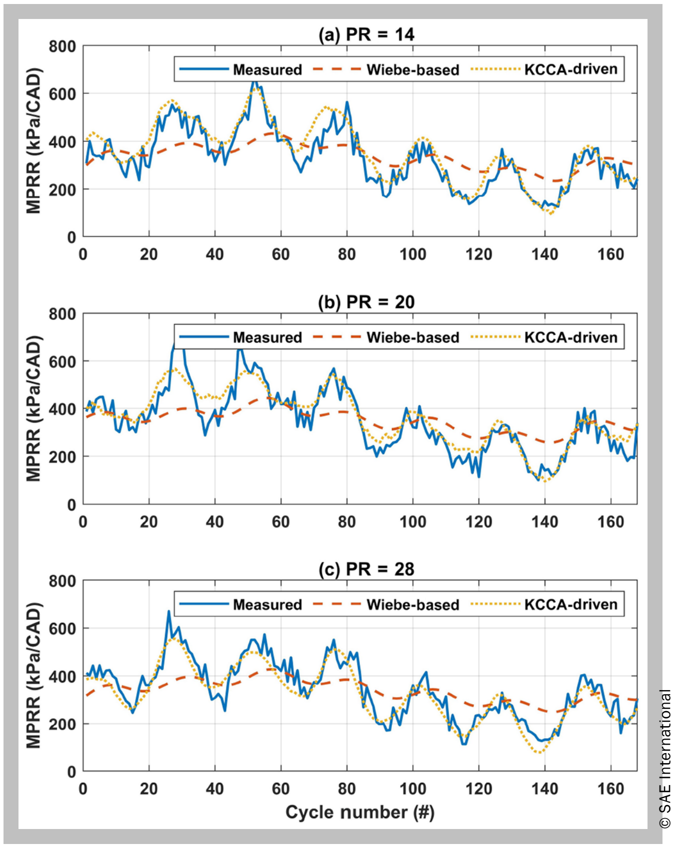

Moreover, these models are accurate enough to be&used in MPRR control applications since MPRR at RCCI engines should be&below 10 bar/CAD [39] and estimation errors for Wiebe-based and KCCA-LPV MPRR models are less than 9% and 4.8% of the allowable MPRR value, respectively.

Summary!and!Conclusions

"is article developed and demonstrated two control-oriented MPRR models for a 2-liter 4-cylinder RCCI engine. " e %rst MPRR model is developed based on a physics-based Wiebe method while the second model is obtained through a data-driven KCCA modeling approach. " e %rst MPRR model simulated the in-cylinder PRR through the %rst law of thermodynamics implementation and calibrated the model by adjusting a Wiebe function, which represents fuel heat release rate. Test results showed that the Wiebe-based MPRR model can estimate experimental MPRR with a mean estimation error of 87 kPa/CAD. In the second MPRR model, unknown states are estimated by the KCCA method, and state-space representations of the RCCI combustion dynamics are computed by the LPV method. " e developed KCCA-driven MPRR model could estimate the experimental MPRR values with an average error of 47 kPa/CAD.

" i s study demonstrated the cycle-by-cycle MPRR in RCCI engines can be&modeled through empirical modeling and machine learning approaches. Both of these methods have a very low computational burden due to their empirical and state-space structure. Modeling efforts and estimation accuracy showed that the machine learning algorithm can provide signi%cantly higher estimation accuracy compared to empirical modeling. "is superior performance of the data-driven model is due to the implementation of highly nonlinear support vector machines to learn the stochastic behavior of the MPRR in RCCI engines. " i s research can be&advanced by employing the proposed MPRR models for developing MPRR controller and expanding the high load operation of RCCI engines.

Contact Information

Behrouz Khoshbakht Irdmousa
bkhoshi@mtu.edu

Definitions/Abbreviations

CA50 - Crank angle for 50% fuel burnt (CAD aTDC)
COV$_{IMEP}$ - Coe$cient of variation of IMEP (%)
e - Estimation or tracking error
E - Stochastic white noise
EOC - End of combustion (CAD aTDC)
EVC - Exhaust valve closing (CAD aTDC)
FQ - Fuel injected per cycle (mg/cycle)
$\mathcal{H}$ - Forward Toeplitz matrix
IMEP - Indicated mean e!ective pressure (kPa)
IVC - Inlet valve closing timing (CAD aTDC)
IVO - Inlet valve opening timing (CAD aTDC)
J - Least-square cost function
k - Gaussian kernel function
LHV - Lower heating value (kJ/kg)
m - Injected fuel mass (kg)
MPRR - Maximum pressure rise rate (kPa/CAD)
Q - Heat release (kJ)
PR - Premixed ratio of dual fuels (-)
PRR - Pressure rise rate (kPa/CAD)
$\mathcal{R}$ - Reachability matrix
SOI - n-heptane injection timing (CAD bTDC)
T$_{in}$ - Temperature at inlet valve closing (K)
T$_{soc}$ - Temperature at start of combustion (K)

U - RCCI engine inputs

W - Support vector weighting matrix

X - RCCI engine states

$\boldsymbol{\alpha}$, $\boldsymbol{\beta}$, $\boldsymbol{\kappa}$, $\boldsymbol{\eta}$ - Lagrange multipliers

$\boldsymbol{\theta}$ - Crank angle (degree)

$\boldsymbol{\gamma}$ - Heat capacity ratio

$\boldsymbol{\lambda}$ - First-stage Wiebe function fraction

$\boldsymbol{\Phi}$ - Feature map function

References

AQ03

1. Reitz, R.D. and Kokjohn, S.L., "Comparison of Conventional Diesel and Reactivity Controlled Compression Ignition (RCCI) Combustion in a Light-Duty Engine," Presentation at 2012 Directions in Engine-E(ciency and Emissions Research (DEER) Conference, Dearborn, MI, 2012.
2. Khameneian, A., "Model-Based Engine-Out Emissions Analysis for a Gasoline Turbocharged Direct Injection Spark-Ignited Engine in Elevated HEV Cranking Speed," PhD thesis, Michigan Technological University, 2021.
3. Khameneian, A., Wang, X., Dice, P., Naber, J.D. et al., "A Real-Time Control-Oriented Discrete Nonlinear Model Development for In-Cylinder Air Charge, Residual Gas and Temperature Prediction of a Gasoline Direct Injection Engine Using Cylinder, Intake and Exhaust Pressures," Control Engineering Practice 119 (2022): 104978.
4. Nazemi, M. and Shahbakhti, M., "Modeling and Analysis of Fuel Injection Parameters for Combustion and Performance of an RCCI Engine," Applied Energy 165 (2016): 135-150.
5. Ansari, E., Poorghasemi, K., Irdmousa, B., Shahbakhti, M. et al., "E$ciency and Emissions Mapping of a Light Duty Diesel-Natural Gas Engine Operating in Conventional Diesel and RCCI Modes," SAE Technical Paper 2016-01-2309, 2016, https://doi.org/10.4271/2016-01-2309.
6. Hellstrom, E., Larimore, J., Jade, S., Stefanopoulou, A.G. et al., "Reducing Cyclic Variability While Regulating Combustion Phasing in a Four-Cylinder HCCI Engine," IEEE Transactions on Control Systems Technology 22, no. 3 (2013): 1190-1197.
7. Zhang, S., Zhu, G., and Sun, Z., "A Control-Oriented Charge Mixing and Two-Zone HCCI Combustion Model," IEEE Transactions on Vehicular Technology 63, no. 3 (2013): 1079-1090.
8. Shaver, G.M., Roelle, M., and Gerdes, J.C., "A Two-Input Two-Output Control Model of HCCI Engines," in 2006 American Control Conference, Minneapolis, MN, 6, IEEE, 2006.
9. Olsson, J.-O., Tunestål, P., and Johansson, B., "Closed-Loop Control of an HCCI Engine," SAE Transactions 110 (2001): 1076-1085.
10. Ebrahimi, K. and Koch, C.B., "Real-Time Control of HCCI Engine Using Model Predictive Control," in 2018 Annual American Control Conference (ACC), Milwaukee, WI, 1622-1628, IEEE, 2018.
11. Shahbakhti, M. and Koch, C.R., "Control Oriented Modeling of Combustion Phasing for an HCCI Engine," in 2007 American Control Conference, New York, 3694-3699, IEEE, 2007.
12. Reitz, R.D. and Duraisamy, G., "Review of High E$ciency and Clean Reactivity Controlled Compression Ignition (RCCI) Combustion in Internal Combustion Engines," Progress in Energy and Combustion Science 46 (2015): 12-71.
13. Irdmousa, B.K., Naber, J.D., Velni, J.M., Borhan, H. et al., "Input-Output Data-Driven Modeling and MIMO Predictive Control of an RCCI Engine Combustion," IFAC-PapersOnLine 54, no. 20 (2021): 406-411.
14. Irdmousa, B.K., Rizvi, S.Z., Veini, J.M., Nabert, J. et al., "Data-Driven Modeling and Predictive Control of Combustion Phasing for RCCI Engines," 2019 American Control Conference (ACC), Philadelphia, PA, 1617-1622, 2019.
15. Sjöberg, M., Dec, J.E., and Cernansky, N.P., "Potential of "ermal Strati%cation and Combustion Retard for Reducing Pressure-Rise Rates in HCCI Engines, Based on Multi-Zone Modeling and Experiments," SAE Transactions 114 (2005): 236-251.
16. Ozaki, J. and Iida, N., "E!ect of Degree of Unmixedness on HCCI Combustion Based on Experiment and Numerical Analysis," SAE Transactions 115 (2006): 1053-1060.
17. Shirota, D. and Iida, N., "An Investigation of the Potential of "ermal and Mixing Strati%cations for Reducing Pressure Rise Rate on HCCI Combustion by Using Rapid Compression Machine," SAE Technical Paper 2009-32-0085, 2009, https://doi.org/10.4271/2009-32-0085.
18. Jung, D., Kwon, O., and Lim, O.T., "Comparison of DME HCCI Operating Ranges for the "ermal Strati%cation and Fuel Strati%cation Based on a Multi-Zone Model," Journal of Mechanical Science and Technology 25, no. 6 (2011): 1383-1390.
19. Shigetoyo, K., Nagae, M., Iino, H., and Iida, N., "An Investigation of Combustion Robustness of HCCI Engines at Retarded Combustion Phasing Operation (by Use of Numerical Analysis with Multi Zone Model)," Nihon Kikai Gakkai Ronbunshu, B Hen/Transactions of the Japan Society of Mechanical Engineers, Part B 76, no. 761 (2010): 142-148.
20. Zheng, Z. and Yao, M., "Charge Strati%cation to Control HCCI: Experiments and CFD Modeling with n-Heptane as Fuel," Fuel 88, no. 2 (2009): 354-365.
21. Zoldak, P., Sobiesiak, A., Bergin, M., and Wickman, D.D., "Computational Study of Reactivity Controlled Compression Ignition (RCCI) Combustion in a Heavy-Duty Diesel Engine Using Natural Gas," SAE Technical Paper 2014-01-1321, 2014, https://doi.org/10.4271/2014-01-1321.
22. Korkmaz, M., Lakshmanan, R., Falkenstein, T., Beeckmann, J. et al., "Experimental and Numerical Investigation of the Maximum Pressure Rise Rate for an LTC Concept in a Single Cylinder CI Engine," SAE Technical Paper 2019-24-0023, 2019, https://doi.org/10.4271/2019-24-0023.

23. Kugimachi, Y., Nakamura, Y., and Iida, N., “Model-Based Combustion Control of a HCCI Engine Using External EGR and the Exhaust Rebreathed,” SAE Technical Paper 2014-32-0079, 2014, https://doi.org/10.4271/2014-32-0079.
24. Hayashi, T., Yamasaki, Y., Miyoshi, M., Kaneko, S. et al., “Study on a Control-Oriented Model of Boosted HCCI Engine and Control Simulation,”) e Proceedings of the International Symposium on Diagnostics and Modeling of Combustion in Internal Combustion Engines 9 (2017): C111.
25. Yang, T., Yin, L., Long, W., Tunestål, P. et al., “Modeling and Control of Gasoline PPC Engine Approaching High E$ciency with Constraints,” IFAC-PapersOnLine 51, no. 31 (2018): 442-447.
26. Basina, L.A., Irdmousa, B.K., Velni, J.M., Borhan, H. et al., “Data-Driven Modeling and Predictive Control of Maximum Pressure Rise Rate in RCCI Engines,” 2020 IEEE Conference on Control Technology and Applications (CCTA), Montreal, QC, Canada, 94-99, 2020.
27. Pan, W., Korkmaz, M., Beeckmann, J., and Pitsch, H., “Unsupervised Learning and Nonlinear Identi%cation for Incylinder Pressure Prediction of Diesel Combustion Rate Shaping Process,” IFAC-PapersOnLine 52, no. 29 (2019): 199-203.
28. Huang, Q., Liu, J., Ulishney, C., and Dumitrescu, C.E., “On the Use of Arti%cial Neural Networks to Model the Performance and Emissions of a Heavy-Duty Natural Gas Spark Ignition Engine,” International Journal of Engine Research 23, no. 11 (2022): 1879-1898.
29. Mishra, C. and Subbarao, P., “Design, Development and Testing a Hybrid Control Model for RCCI Engine Using Double Wiebe Function and Random Forest Machine Learning,” Control Engineering Practice 113 (2021): 104857.
30. Shin, S., Lee, S., Kim, M., Park, J. et al., “Deep Learning Procedure for Knock, Performance and Emission Prediction at Steady-State Condition of a Gasoline Engine,” Proceedings of the Institution of Mechanical Engineers, Part D: Journal of Automobile Engineering 234, no. 14 (2020): 3347-3361.
AQ04 31. Liu, J., Ulishney, C., and Dumitrescu, C.E., “Prediction of E$cient Operating Conditions inside a Heavy-Duty Natural Gas Spark Ignition Engine Using Arti%cial Neural Networks,” in ASME International Mechanical Engineering Congress and Exposition, vol. 84560 (New York: American Society of Mechanical Engineers, 2020), V008T08A013.
32. Maldonado, B., Kaul, B., Schuman, C., Young, S. et al., “Dilute Combustion Control Using Spiking Neural Networks,” SAE Technical Paper 2021-01-0534, 2021, https://doi.org/10.4271/2021-01-0534.
33. Schuman, C.D., Young, S.R., Maldonado, B.P., and Kaul, B.C., “Real-Time Evolution and Deployment of Neuromorphic Computing at the Edge,” 2021 12th International Green and Sustainable Computing Conference (IGSC), Pullman, WA, 1-8, 2021.
34. Maldonado, B., Stefanopoulou, A., and Kaul, B., “Arti%cial-Intelligence-Based Prediction and Control of Combustion Instabilities in Spark-Ignition Engines,” in Arti*cial Intelligence and Data Driven Optimization of Internal Combustion Engines (Amsterdam, the Netherlands: Elsevier, 2022), 185-212.
35. Heywood, J.B., Internal Combustion Engine Fundamentals (New York: McGraw-Hill Education, 2018), Chapter 3.
36. Woschni, G., “A Universally Applicable Equation for the Instantaneous Heat Transfer Coe$cient in the Internal Combustion Engine,” SAE Technical Paper 670931, 1967, https://doi.org/10.4271/670931.
37. Rizvi, S.Z., Velni, J.M., Abbasi, F., Tóth, R. et al., “State-Space LPV Model Identi%cation Using Kernelized Machine Learning,” Automatica 88 (2018): 38-47.
38. Rizvi, S.Z., Mohammadpour, J., Tóth, R., and Meskin, N., “A Kernel-Based Approach to MIMO LPV State-Space Identi%cation and Application to a Nonlinear Process System,” IFAC-PapersOnLine 48, no. 26 (2015): 85-90.
39. Curran, S., Gao, Z., and Wagner, R., “Reactivity Controlled Compression Ignition Drive Cycle Emissions and Fuel Economy Estimations Using Vehicle Systems Simulations with E30 and ULSD,” SAE Int. J. Engines 7, no. 2 (2014): 902-912, doi:https://doi.org/10.4271/2014-01-1324.